



UNIVERSITÀ POLITECNICA DELLE MARCHE
Repository ISTITUZIONALE

Structural characterization of biomedical Co-Cr-Mo components produced by Direct Metal Laser Sintering.

This is the peer reviewed version of the following article:

Original

Structural characterization of biomedical Co-Cr-Mo components produced by Direct Metal Laser Sintering / Barucca, Gianni; Santecchia, Eleonora; Majni, Giuseppe; Girardin, Emmanuelle; Elena, Bassoli; Lucia, Denti; Andrea, Gatto; Luca, Iuliano; Tomasz, Moskalewicz; Mengucci, Paolo. - In: MATERIALS SCIENCE AND ENGINEERING. C, BIOMIMETIC MATERIALS, SENSORS AND SYSTEMS. - ISSN 0928-4931. - ELETTRONICO. - 48:(2015), pp. 263-269. [10.1016/j.msec.2014.12.009]

Availability:

This version is available at: 11566/221915 since: 2022-06-23T07:45:11Z

Publisher:

Published

DOI:10.1016/j.msec.2014.12.009

Terms of use:

The terms and conditions for the reuse of this version of the manuscript are specified in the publishing policy. The use of copyrighted works requires the consent of the rights' holder (author or publisher). Works made available under a Creative Commons license or a Publisher's custom-made license can be used according to the terms and conditions contained therein. See editor's website for further information and terms and conditions.

This item was downloaded from IRIS Università Politecnica delle Marche (<https://iris.univpm.it>). When citing, please refer to the published version.

(Article begins on next page)

Structural characterization of biomedical Co-Cr-Mo components produced by Direct Metal Laser Sintering

G. Barucca ^{a,*}, E. Santecchia ^a, G. Majni ^a, E. Girardin ^b, E. Bassoli ^c, L. Denti ^c, A. Gatto ^c,
L. Iuliano ^d, T. Moskalewicz ^e, P. Mengucci ^a

^a SIMAU, Università Politecnica delle Marche, via Brecce Bianche, 60131 Ancona, Italy.

^b DISCO, Università Politecnica delle Marche, via Brecce Bianche, 60131 Ancona, Italy.

^c DIMeC, University of Modena and Reggio Emilia, via Vignolese 905/B, Modena 41125, Italy.

^d DISPEA, Politecnico di Torino, C.so Duca degli Abruzzi 24, 10129 Torino, Italy.

^e Faculty of Metals Engineering and Industrial Computer Science, AGH University of Science
and Technology, Al. Mickiewicza 30, 30-059 Kraków, Poland.

* Corresponding author: SIMAU, Università Politecnica delle Marche, via Brecce Bianche,
60131 Ancona, Italy. Tel.: +39 071 2204754; fax: +39 071 2204729.

E-mail address: g.barucca@univpm.it (G. Barucca).

ABSTRACT

Direct Metal Laser Sintering (DMLS) is a technique to manufacture complex functional mechanical parts from a computer-aided design (CAD) model. Usually, the mechanical components produced by this procedure show higher residual porosity and poorer mechanical properties than those obtained by conventional manufacturing techniques.

In this work, a Co-Cr-Mo alloy produced by DMLS with a composition suitable for biomedical applications was submitted to hardness measurements and structural characterisation. The alloy showed a hardness value remarkably higher than those commonly obtained for the same cast or wrought alloys. In order to clarify the origin of this unexpected result, the samples microstructure was investigated by X-ray diffraction (XRD), electron microscopy (SEM and TEM) and energy dispersive microanalysis (EDX). For the first time, a homogeneous microstructure comprised of an intricate network of thin ϵ (hcp)-lamellae distributed inside a γ (fcc) phase was observed. The ϵ -lamellae grown on the $\{111\}_{\gamma}$ planes limit the dislocation slip inside the γ (fcc) phase, causing the measured hardness increase. The results suggest possible innovative applications of the DMLS technique to the production of mechanical parts in the medical and dental fields.

KEYWORDS: metals and alloys; laser processing; sintering; transmission electron microscopy, TEM; scanning electron microscopy, SEM; X-ray diffraction.

1. INTRODUCTION

Nowadays, a new class of manufacturing methods are becoming increasingly important for the production of biomedical devices. Among them, novel methods based on additive manufacturing (AM), assisted by computer-aided design/computer-aided manufacturing (CAD/CAM), allow the production of intricate mechanical parts [1-4].

Direct metal laser sintering (DMLS) is an AM process that uses the heat of a solid state laser to sinter metal powder particles [5]. In this case, a distribution mechanism pre-places successive layers of powder on a suitable substrate, while a laser beam controlled by a scanning system locally sinters the powder in accordance with the CAD model [6]. This technology, like other AM procedures, is highly rewarding in medicine where a high degree of personalization is required [7-9]. Prosthetic applications are particularly well suited for processing by means of DMLS due to their complex geometry, low volume and strong individualization [10]. Furthermore, the manufacturing of multiple unique parts in a single production run enables extensive customization with a strong reduction of manual operation leading to higher repeatability and good savings in money and delivery times.

Cobalt-based alloys were extensively used in cast and hard facing forms over the past twenty years because of their corrosion and wear resistance, biocompatibility and excellent strength and toughness at high temperature [11]. Typical applications of the Co-based alloys involved both the biomedical and the metallurgical fields [12, 13].

From a structural point of view, cobalt is characterized by a ϵ (hcp) low temperature phase and a γ (fcc) phase at higher temperature. The addition of chromium improves the corrosion and the oxidation resistance of the alloy, as well as its hardness, ductility and wear resistance through

carbide formation. Molybdenum improves the corrosion resistance and acts as a solid-solution strengthener by forming the Co_3Mo (hcp) intermetallic compound [14].

Cast alloys with a Cr content ranging from 19 wt% to 30 wt% and a Mo content in the range 5-10 wt% were considered for biomedical applications and for many years these compositions were used to produce medical implants such as hips, knees, ankles and bone plates [15].

Although in the past few years, several AM techniques were applied to produce biocompatible Co-based alloys, only in few cases a deep microstructural characterisation of the sintered components were performed. In particular, Gaytan et al. reported on the microstructure and the mechanical properties of Co-based prototypes produced by electron beam melting. In this study, they found high hardness values attributed to the formation of an ordinate array of metal carbides [16]. Meacock et al. investigated the microstructure and the mechanical properties of a biomedical Co-Cr-Mo alloy produced by laser powder microdeposition [17]. They observed a homogenous microstructure comprised of fine cellular dendrites and measured an average hardness value of 460 $\text{HV}_{0.02}$, well higher than the typical values obtained by other fabrication processes. From these results, they concluded that the fine morphology is responsible of the significantly increased hardness value.

Few other papers deal with the possibility of realizing medical parts of a Co-Cr-Mo alloy by the DMLS technique, but it is worth to note that none of them reports on the correlation of the samples microstructure to the mechanical properties of the final components as well as detailed transmission electron microscopy analyses [19-21].

The mechanical properties of the sintered components are strictly linked to the samples microstructure and are one of the major aspects connected to the practical applications of the AM procedures. Usually, objects produced by metal powder sintering show poorer mechanical

properties than those produced by conventional procedures. This behaviour is mainly due to the fact that DMLS, depending on the laser energy density employed, involves a partial or total melting of the powder. Therefore, the products made by DMLS could show high surface roughness, porosity (in certain cases even lack of densification), heterogeneous microstructure and thermal residual stresses that may give rise to poor mechanical properties [22].

In this paper, metallic components of a biocompatible Co-Cr-Mo alloy produced by the DMLS technique were deeply investigated in order to correlate their hardness behaviour to the corresponding microstructure. To this aim, hardness measurements, X ray diffraction (XRD) analysis, electron microscopy (SEM, TEM) observations and energy dispersive microanalysis (EDX) were performed on the samples. Results evidenced a surprisingly high hardness value of the investigated Co-Cr-Mo alloy in comparison of the hardness values commonly reported in literature for similar compositions. This unexpected result was attributed to the peculiar microstructure observed in the analysed samples, that, to our knowledge, was never reported before.

2. MATERIALS AND METHODS

2.1 Material composition and sintering parameters

Specimens were prepared by direct metal laser sintering using a Yb (ytterbium) fiber laser system (EOSINT-M270) operating with the standard deposition parameters reported in Table 1.

Table 1

Parameters used for DMLS

| | |
|-----------------------|-------------------------|
| laser power | 200W |
| laser spot diameter | 0.200 mm |
| Scan speed | up to 7.0 m/s |
| Building speed | 2-20 mm ³ /s |
| Layer thickness | 0.020 mm |
| Protective atmosphere | max 1.5% oxygen |

A Co-Cr-Mo alloy powder (EOS Cobalt/Chrome SP2) with the nominal composition (in wt%) Co 63.8, Cr 24.7, Mo 5.1, W 5.4, Si 1.0, was used as raw material. The powder is free of Ni, Be and Cd according to EN ISO 22674. The nominal composition was provided by the manufacturer (EOS GmbH Electro Optical Systems). The powder is the EOS Cobalt/Chrome SP2 cobalt based metal ceramic alloy intended for production of Porcelain-Fused to Metal (PFM) dental restorations (crowns, bridges, etc.) in EOSINT M 270 Standard installation mode. The powder is class IIa medical device in accordance with annex IX rule 8 of the MDD 93/42/EEC. Composition corresponds to “type 4” CoCr dental material according to EN ISO 22674. Rectangular parallelepipeds with size 250 mm x 4 mm and a thickness of 6 mm were sintered by using the parameters reported in Table 1. In order to minimize anisotropy, each layer was built with the laser scanning along a specific direction. Layer-by-layer the scanning direction was rotated by 25° with respect to the previous one.

2.2 Hardness measurements

Hardness tests were performed on the sintered samples using the Rockwell scale C (specifications ISO 4498 : Sintered metal materials, excluding hard metals - Determination of apparent hardness and microhardness). Measurements were obtained averaging five indentations following ISO 6508: Rockwell hardness test.

2.3 Structural characterisation

Structural and microstructural characterizations were carried out by X-ray diffraction (XRD), scanning (SEM) and transmission (TEM) electron microscopy techniques.

XRD measurements were performed by a Bruker D8 Advance diffractometer operating with a Cu-K α radiation source at V= 40kV and I= 40 mA in the angular range $2\theta=10 - 90^\circ$.

SEM analyses were carried out by a ZEISS SUPRA 40 microscope equipped with a Bruker Quantax energy dispersive X-ray microanalysis (EDX). Observations were performed on both the as-received metallic powder and cross-sectioned sintered samples. Before observations, samples surfaces were prepared using a conventional metallographic procedure and electrochemically etched in the following conditions: HCl 0.1 M, 2V, 2 min.

TEM analyses were carried out by a Philips CM200 electron microscope operating at 200 kV and by a JEOL JEM-2010 ARP microscope equipped with an Oxford Inca energy dispersive X-ray microanalysis (EDX). For TEM observations, samples were prepared by the conventional thinning procedure consisting of mechanical polishing by grinding papers, diamond pastes and a dimple grinder. Final thinning was carried out by an ion beam system (Gatan PIPS) using Ar ions at 5 kV.

3. RESULTS

3.1 Hardness

The average Rockwell C hardness (HRC) value measured for the laser sintered samples is 47 HRC, a very high value considering that the usual range for cast Co-Cr-Mo alloys is from 25 to 35 HRC.

3.2 X-ray diffraction (XRD)

X-ray diffraction measurements were performed on both the Co-Cr-Mo powder used as raw material for the DMLS process and on the different regions of the sintered samples (Fig. 1).

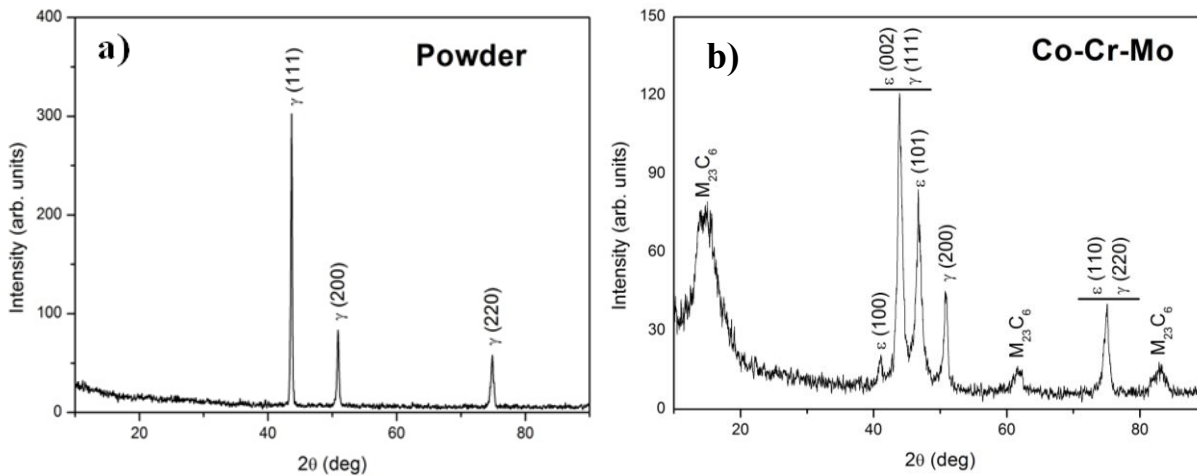


Fig. 1. X-ray diffraction patterns: a) as-received metallic powder; b) sintered sample.

Fig. 1a reports the XRD pattern of the as-received metallic powder. All the visible peaks can be attributed to the cubic cobalt phase, commonly referred to as γ phase. The γ phase has a face centred cubic (fcc) lattice with a nominal parameter $a=0.35447$ nm (ICDD card n. 15-806). For the alloy under study, the best fit performed by using the three diffraction peaks of Fig. 1a provides a lattice parameter value $a=0.3586$ nm, in close agreement with the values reported in literature for alloys of similar composition [23].

The XRD pattern of the sintered sample is shown in Fig. 1b. The most intense and well-defined peaks are a result of the simultaneous presence of both γ and ϵ cobalt phases, as indicated in Fig. 1b where each diffraction peak is indexed with the name of the corresponding Co phase. A double indexation is reported for the most intense peak at $2\theta=43.94^\circ$ and the peak at $2\theta=75.09^\circ$ because of the superposition of the reflections due to the ϵ and γ phases. The ϵ phase has a hexagonal close packed (hcp) lattice with nominal parameters $a=0.25031$ nm and $c=0.40605$ nm (ICDD card n. 5-727). By using the ϵ (100) and ϵ (101) peaks of the XRD pattern shown in Fig. 1b, the lattice parameters of the hexagonal ϵ phase formed in our alloy were determined to be $a=0.2539$ nm and $c=0.4122$ nm with a c/a ratio of 1.623. The lattice parameter of the fcc γ phase formed in the sintered sample evaluated by the γ (200) peak of Fig. 1b is $a=0.3589$ nm. Also in this case, the calculated lattice parameters for the ϵ and γ phases formed in our alloy are in close agreement with those reported in literature for similar compositions [23].

In order to estimate the volume fraction of the hcp and fcc cobalt phases in the sintered sample, the integrated intensities of the γ (200) and ϵ (101) peaks were used. The quantitative determination, performed by using the method of Sage and Gillaud [24], resulted in an ϵ -phase volume fraction $f_{\text{hcp}}=0.49\pm0.03$.

In addition to the ϵ and γ peaks in Fig. 1b, three broad peaks attributable to metals carbides are also visible. These latter peaks generically indexed as $M_{23}C_6$ ($M=\text{Cr, Co, Mo, W}$) are due to metal carbides having the cubic structure of the Cr_{23}C_6 compound (ICDD card n. 35-783).

3.3 Scanning electron microscopy (SEM) and microanalysis (EDX)

Scanning electron microscopy observations were performed on the as-received powder and on the sintered samples. Particles forming the metallic powder are shown in Fig. 2.

From the SEM images the average size of the spherical particles were evaluated. Measurements were performed by averaging the data obtained from different areas of the samples. Results showed that the size of the particles ranges from 4 to 80 μm .

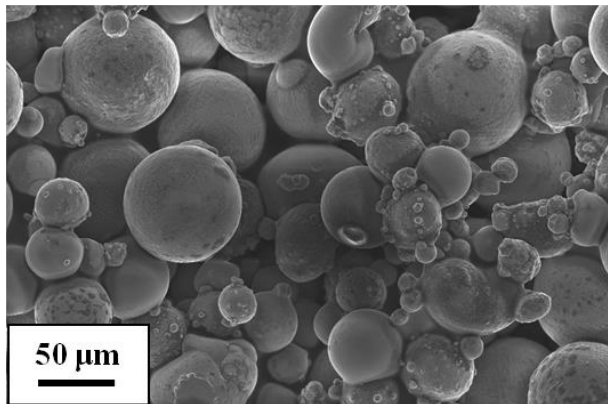


Fig. 2. SEM image of the as-received metallic powder.

EDX analysis performed on the powder showed a chemical composition in agreement with the nominal composition of the alloy reported above. In Table 2 the experimental values obtained from the EDX analyses performed on the powder and on the sintered sample are reported.

Table 2

Experimental results of the EDX microanalysis performed on both the powder and the sintered sample.

| Element | Powder (wt%) | Sintered sample (wt%) |
|---------|--------------|-----------------------|
| Co | 62 | 63 |
| Cr | 26 | 26 |
| Mo | 5 | 6 |
| W | 4 | 4 |
| Si | 1 | 1 |

It is worth to note that the average composition of the powder and the sintered sample is almost the same, as can be inferred from Table 2.

The inner structure of the sintered samples, as observed by SEM, is shown in Fig. 3. Samples were sectioned parallel to the laser beam direction, and SEM observations were performed after a metallographic preparation of the surfaces followed by an electrochemical etching. The lines separating the different weld pools produced by the laser scan on each layer are evidenced by arrows in the image taken at low magnification, Fig. 3a.

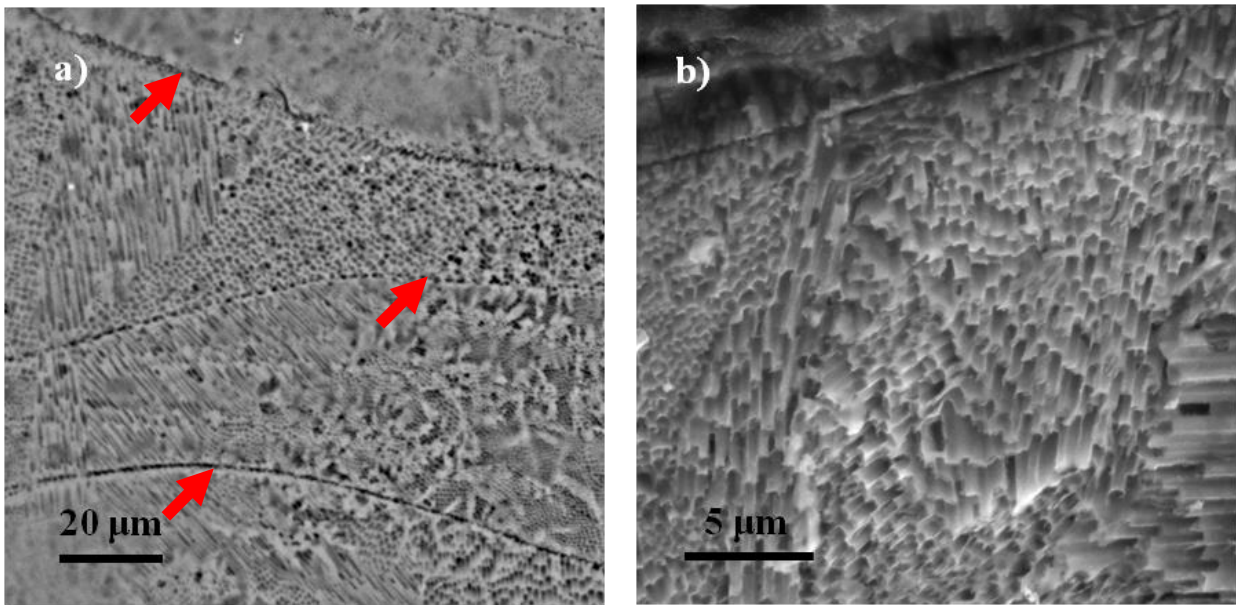


Fig. 3 SEM images of the sintered samples. a) low magnification: lines separating different weld pools are arrowed; b) high magnification.

Observations performed at higher magnification allow to evidence the presence of an extremely fine microstructure inside a single pool, Fig. 3b. Columnar structures, with diameters ranging from 300 to 400 nm and heights from 4 to 8 μm, grow inside the matrix in form of domains. The orientation of the columns is the same inside a single domain while it changes from one domain to the other. In order to estimate the area fraction occupied by the columnar structures relative to

the matrix, several SEM images were processed by using an image analysis software [25]. An area fraction of $45 \pm 5\%$ was provided by software. This value, as a rough approximation, can be considered as the volume fraction of the columnar structures relative to the rest of the sample.

3.4 Transmission electron microscopy (TEM) and microanalysis (EDX)

TEM observations of the sintered samples confirm the presence of the two ϵ and γ cobalt phases. The ϵ phase forms as small lamellae inside the γ phase. The thickness of the ϵ phase lamellae is 1-2 nm, but in some cases, they tend to aggregate in the same region of the sample forming alternate structures of ϵ and γ phases with lateral dimensions of up to 400 nm.

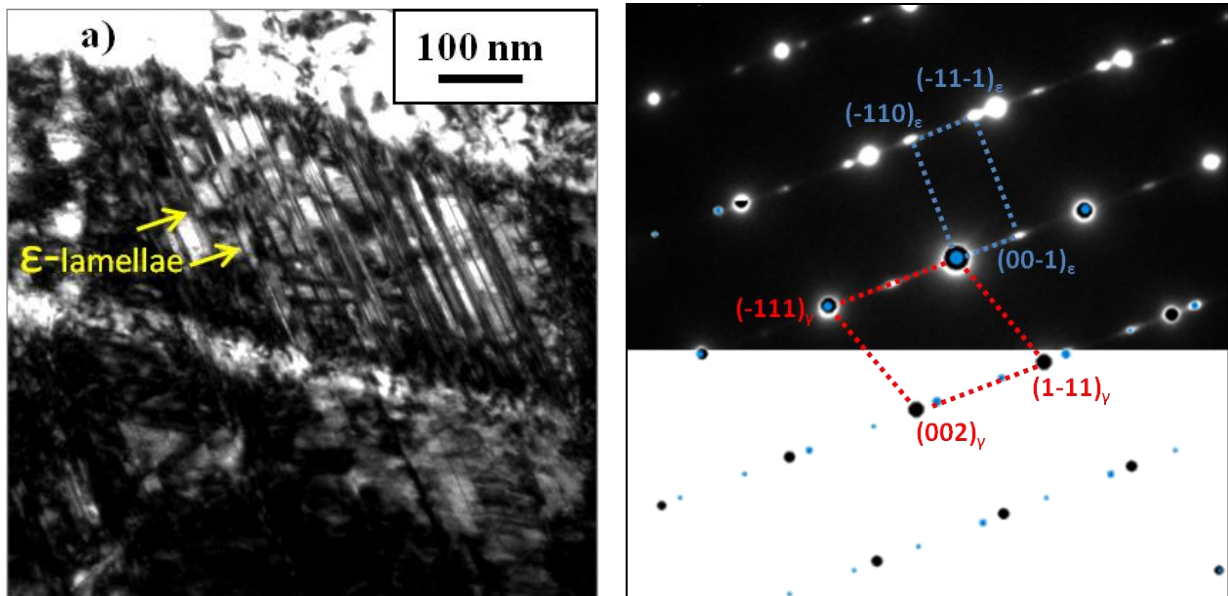


Fig. 4. Sintered sample: a) TEM bright field image of the ϵ lamellae inside the γ phase (arrowed); b) SAD pattern taken in the same area in $\langle 110 \rangle_\gamma$ zone axis orientation (upper part) and corresponding software simulation (lower part). In red is indicated the cell of the γ -Cobalt phase and in blue the cell of the ϵ -Cobalt phase.

223 In Fig. 4a, taken in $\langle 110 \rangle_\gamma$ zone axis orientation, the lamellar structure is clearly visible. The
 224 lamellae are parallel to each other, and the distance between them is not constant. Considering
 225 the ensemble of these lamellae, it is possible to envisage one of the columnar structures visible in
 226 the SEM images. The corresponding selected area diffraction (SAD) pattern is reported in the
 227 upper part of Fig. 4b while its simulation performed with the CrystalKitX software [26] is shown
 228 in the lower part of Fig. 4b. The remarkable agreement between the simulated pattern and the
 229 experimental one is evident. The most intense spots visible in Fig. 4b (top) are a result of the fcc
 230 γ -phase (red cell) while the smaller ones are a result of the hcp ϵ -phase (blue cell). The geometry
 231 of the spot distribution in the SAD pattern of Fig. 4b (top) reveals that the ϵ lamellae form with
 232 the following orientation relationships with the γ matrix:

$$\begin{aligned} 233 \quad & \{001\}_\epsilon // \{111\}_\gamma \\ 234 \quad & \langle 100 \rangle_\epsilon // \langle 1-10 \rangle_\gamma \end{aligned}$$

235 Furthermore, as can be observed in Fig. 4b (top), the spots of the ϵ phase are streaked in direction
 236 of the $\{111\}_\gamma$ spots indicating that the lamellae grow on the $\{111\}_\gamma$ lattice planes and have a
 237 small thickness in the $\langle 111 \rangle_\gamma$ lattice direction.

238 In order to investigate the spatial distribution of the hcp lamellae in greater details, TEM
 239 observations were also performed in the $\langle 111 \rangle_\gamma$ zone axis orientation.

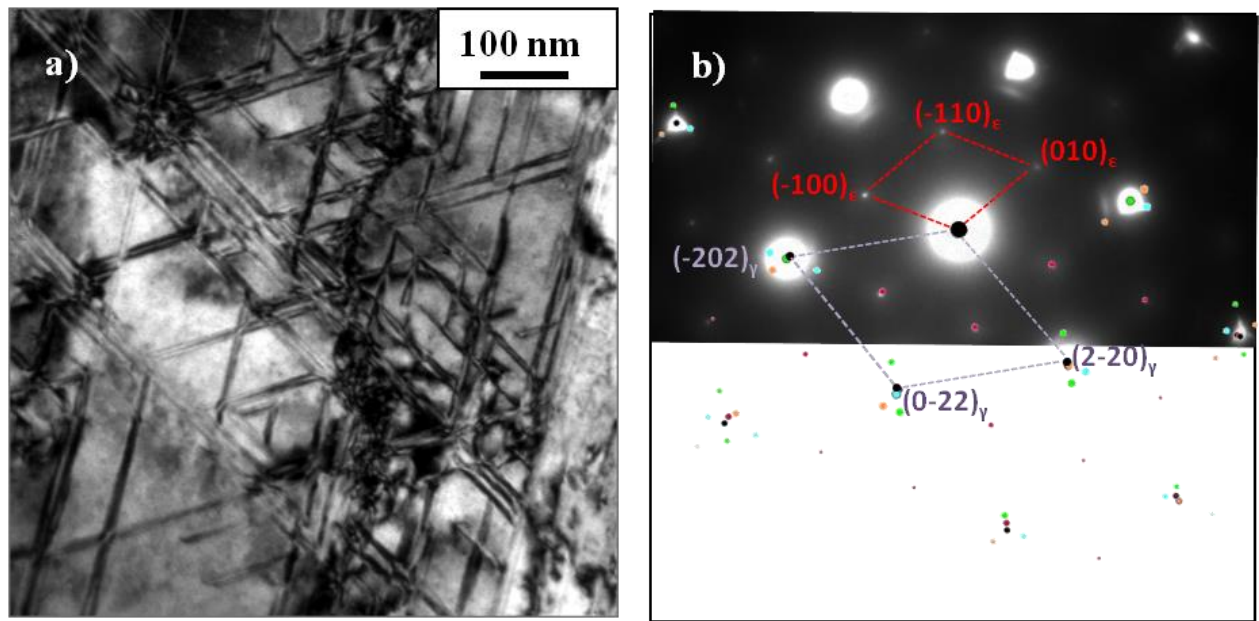
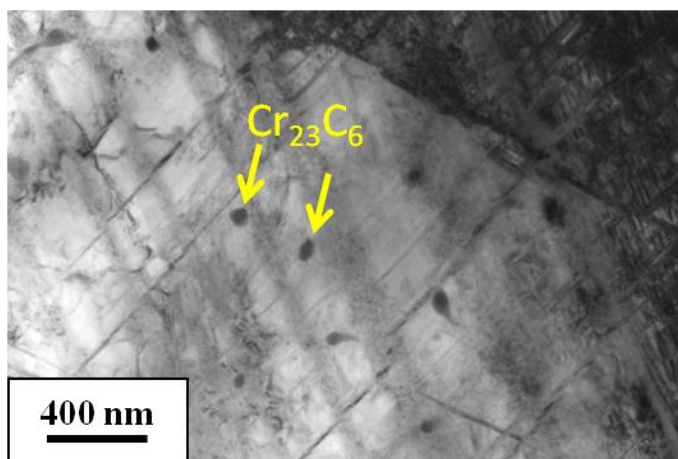


Fig. 5. Sintered sample: a) bright field TEM image taken in $\langle 111 \rangle_\gamma$ zone axis orientation; b) corresponding SAD pattern (upper part) and software simulation (lower part). In red is indicated the cell of the ϵ -Cobalt phase in one of the four possible orientations on the $\{111\}_\gamma$ lattice planes, and in violet the cell of the γ -Cobalt phase.

A bright field image of the sample in this orientation is shown in Fig. 5a. Lamellae and stacking faults lying on different $\{111\}_\gamma$ lattice planes are visible and form an intricate network. The corresponding SAD pattern, with the simulation performed by the CrystalKitX software, are shown in the upper and lower part of Fig. 5b, respectively. The SAD pattern was simulated considering the four possible orientations of the ϵ phase on the $\{111\}_\gamma$ lattice planes. Different colours correspond to different orientations. In particular the diffraction spots corresponding to the $(001)_\epsilon // (111)_\gamma$ orientation were indexed in Fig. 5b and indicated with the red cell.

It must be stressed that all the SAD patterns, taken even in other orientations, never showed the presence of twins reflections ($1/3 \langle hkl \rangle$), although at a first glance the ϵ lamellae could be confused with microtwins.

255 TEM observations performed on the sintered samples also revealed the presence of small
256 quantities of precipitates uniformly distributed. Precipitates, visible as dark dots inside the matrix
257 in Fig. 6, have a spherical or elliptical shape with size ranging from 50 to 300 nm.



258 **Fig. 6.** TEM bright field image of the sintered sample showing the presence of some metal
259 carbides (arrowed).

260
261 In order to investigate the chemical composition of these precipitates, EDX measurements were
262 performed. Results show an increase of the Cr, W and Mo content in the precipitates with respect
263 to the matrix, while the precipitates composition remains almost the same independently of their
264 shape, Table 3. The crystallographic nature of the precipitates was investigated by the SAD
265 technique. Results are compatible with the presence of a phase having the Cr_{23}C_6 lattice
266 structure.

Table 3

Experimental results of the EDX measurements performed on both the matrix and the precipitates.

| Element | Matrix (wt%) | Precipitates (wt%) |
|---------|--------------|--------------------|
| Co | 63 | 52 |
| Cr | 24 | 26 |
| Mo | 5 | 11 |
| W | 6 | 10 |
| Si | 1 | 1 |

4. DISCUSSION

The hardness values of the laser sintered samples are surprisingly high, considering the method used for their realization. Generally, components produced by an additive manufacturing technique, such as the Direct Laser Metal Sintering procedure used in this work, can be affected by residual porosity and show poorer mechanical properties than those obtained by traditional manufacturing techniques [22]. In our case, however, hardness results to be remarkably high, even if compared to the same cast or wrought alloy. The explanation of this result is linked to the inner structure of the samples, as will be discussed below. Furthermore, it must be stressed that hardness is only one of the mechanical properties playing an important role in material selection for application in the human body [12]. Other quantities such as tensile strength, Young's modulus and elongation must be considered when the application range of a biomaterial is involved. On the other hand, Murr et al. demonstrated the possibility to set the Young's modulus of femoral component constituted of a Co-29Cr-6Mo alloy by opportunely developing mesh and

foam implant prototypes produced by an additive manufacturing technique [27]. This means that the implant design influences also its final mechanical properties.

X-ray diffraction results show a phase transformation connected to the laser treatment. In particular, while the powder is exclusively composed of the γ (fcc) cobalt phase, the sintered sample contains both the γ (fcc) and ϵ (hcp) phases. Cobalt-based alloys undergo an fcc \leftrightarrow hcp martensitic transformation. The equilibrium temperature between the high-temperature γ (fcc) phase and the low-temperature ϵ (hcp) phase is around 970 °C. In pure Co the equilibrium temperature between the two phases is around 427°C [28]. The fcc \rightarrow hcp transformation in Co and its alloys is very sluggish due to the limited chemical driving forces available at the transformation temperature. Thus, under normal cooling conditions, the fcc phase is retained below the phase boundary in a metastable state. The metastable fcc phase can transform to hcp by plastic deformation, by isothermal aging at temperatures between 650 and 950 °C, and athermally, by rapid cooling from the annealing temperatures ($> 1100^\circ\text{C}$) [24,29]. In our samples, the laser beam produces the local melting of the metal powder that rapidly solidifies and cools down due to the high thermal conductivity of the metallic alloy and the smallness of the heated area during the laser treatment. Thus, in the successive small areas treated with the laser beam during the production process is possible to reach a condition very similar to that responsible of the athermal martensitic transformation. Accordingly the athermal martensitic transformation is the origin of the ϵ (hcp) phase in our sintered samples.

SEM observations of the DLMS samples, reveal a complex microstructure. Parallel columnar structures form different domains inside the same melted pool produced by the laser beam. This morphology is very different from the cellular dendritic morphology observed by Meacock et al [17]. They reported on the microstructure and properties of a typical Co-Cr-Mo biomedical alloy

manufactured by laser powder microdeposition (LPMD). Although this latter technique, similarly to the DLMS, involves melting of a small quantity of metal powder by a laser beam followed by a rapid quenching, different microstructures are produced. It must be stressed that the laser sintering process is very complex because it involves multiple modes of heat, mass and momentum transfer, and chemical reactions [5]. As a consequence, it is not too surprising that two different laser sintering techniques produce different final samples microstructure. Gaytan et al. [16] reported on the microstructure and mechanical properties of parts fabricated by electron beam melting (EBM) of a Co-26Cr-6Mo-0.2C powder. They observed hardness values similar to the values experimentally obtained in our work, attributed to the formation of carbides lined up to form columns perpendicular to the build direction. Although the columns of carbides look similar to the columnar structures visible in our SEM images, XRD and TEM analyses show that metal carbides are only present in small quantities and do not form columnar structures in our samples. In particular, TEM observations reveal the formation of ϵ -martensite lamellae inside the fcc-Co grains. These lamellae grow on the $\{111\}$ planes of the cubic γ -phase and tend to aggregate forming the columnar structures visible in the SEM images. Therefore, the columnar structures visible in our SEM images although similar to other structure reported in literature, have a completely different nature, never observed before.

As known, the hcp stacking sequence can be produced by introducing an intrinsic stacking fault on every second (111) plane of an fcc lattice. Furthermore, this can be accomplished by a shearing process if the intrinsic faults are bounded by Shockley $a/6 \langle 112 \rangle$ partial dislocations. This mechanism, invoked in the fcc \rightarrow hcp martensitic transformation [30], explains the orientation relationship between the ϵ and the γ phases experimentally observed in the electron diffraction patterns reported in Fig. 4b. Considering the different families of $\{111\}$ planes, the

presence of different orientations of the columnar structures inside a single melt pool is not surprising.

The estimation of the area fraction occupied by the columnar structures with respect to the matrix, obtained by SEM images elaboration, is comparable with the ϵ -phase volume fractions obtained by XRD spectra analyses. This is in agreement with TEM observations revealing that the columnar structures are due to the aggregation of ϵ -martensite lamellae.

Generally, for a conventional Co-Cr-Mo alloy, the percentage of athermal ϵ -martensite ranges from 10 vol.% to 15vol.% depending on the chemical composition of the alloy, the solution temperature and time, and the cooling rate [28]. Using only conventionally [31] or laser sintered [17] Co-Cr-Mo powders, amounts of athermal ϵ -martensite ranging from 30 vol.% to 70 vol.% were produced. The reason for these large amounts was mainly attributed to a large nucleation of ϵ -embryos promoted by the free surfaces and grain development at powder contact surfaces combined with recrystallization and grain growth within the powder particles, or promoted by the cell grain boundary between the dendritic and interdendritic zone. In our samples, the cellular dendritic morphology was not observed, and the powder particles completely melted during the laser treatment. Thus, it is not possible to invoke in our samples the same mechanisms of nucleation promotion. Furthermore, in the two above-mentioned works, TEM analyses were not performed, therefore it is not possible to compare the distribution and morphology of the ϵ -phase. Comparisons can be performed with the athermal ϵ -martensite present in conventional Co-Cr-Mo alloys [32]. In such case, the ϵ -phase forms thick bands inside the fcc-phase. To our knowledge, the formation of an intricate network of thin ϵ -lamellae, comparable to that of our samples, was never observed before. All this suggests that in the DLMS procedure the cooling rates of the melted powder are so rapid that a lot of lattice defects are formed during

solidification, and these defects exactly represent the ϵ -embryos promoting the martensitic transformation.

For completeness, during the samples sintering, the deposited layers were heated as each successive layer was deposited. These heating treatments could have induced isothermal martensitic transformations in the alloy. However, it is reported in literature that the isothermal martensitic formation is accompanied by the formation of discontinuous rows of carbides connected to the negligible carbon solubility in the hcp phase [30,33]. The spherical carbides present in our samples do not satisfy the features reported above, and they are probably formed during the solidification process.

The HRC hardness values reported for the common cast Co-Cr-Mo alloys range from 25 to 35 HRC. These values are considerably lower than those measured in the part manufactured by DLMS. Furthermore, it was found that the hardness value exhibits a linear increase at the increasing of the ϵ phase content [24]. This latter result can be attributed to the growth of the ϵ -phase on the $\{111\}_{\gamma}$ planes that restrict dislocation slip in the fcc lattice. Moreover, the dislocation slip in the hcp lamellae is also inhibited by the intersection of these hcp lamellae with other hcp ones or with fcc regions [30]. Therefore, all the aforementioned phenomena and the peculiar intricate network of ϵ -lamellae experimentally observed in our samples, can explain the high hardness values obtained. In fact, in our samples the ϵ lamellae grow on the slip plains of the γ -(fcc) phase. The density and the spatial distribution of these ϵ lamellae enormously restrict the dislocations slip, thus increasing the hardness values of our samples.

The presence of metal carbides could even play a role in the strengthening of the alloy by the Orowan mechanism. However, considering the small quantity of carbides observed in our

samples, it is more probable that the main mechanism of strengthening is due to the martensitic transformation induced in the alloy by the DLMS procedure.

The increased hardening manifested in the sintered samples along with the microstructure homogeneity observed could make the direct metal laser sintering technique a very useful and powerful procedure to produce surgical implants from Co-Cr-Mo alloys. In this framework, it must be stressed that high hardness values are particularly desirable in the field of prosthesis applications to reduce the debris due to the friction action in the polyethylene-on-metal artificial joints. As shown by Gonzalez-Mora et al. [34], that studied the role of hardness and roughness on the wear of polyethylene in the polyethylene-on-metal artificial joints, hard surfaces are more resistant against scratching and consequently produces less polyethylene wear, the roughness being not the main parameter.

Future work will involve studies on the correlation between the deposition parameters of the DMLS production process, and the microstructure and the mechanical properties of the final products. Furthermore, additional mechanical tests will be performed on the sintered Co-Cr-Mo samples in order to investigate tensile strength, Young's modulus and elongation.

5. CONCLUSIONS

In the present paper, we reported on the structural and microstructural characterization of Co-Cr-Mo parts produced by Direct Metal Laser Sintering. The composition of the alloy was chosen in order to produce biocompatible parts. Sintered samples were characterized by X-ray diffraction, scanning and transmission electron microscopy and EDS microanalysis. The main results obtained can be listed as follows:

- 1) The laser treatment melts the metallic Co-Cr-Mo powder and induces a phase transformation from the γ (fcc) to the ϵ (hcp) phase;
- 2) The phase transformation is an athermal martensitic transformation and produces an intricate network of thin ϵ -lamellae distributed inside the γ phase. This microstructure was never observed before;
- 3) The large amount of ϵ -lamellae could be attributed to a large nucleation of ϵ -embryos promoted by lattice defects formation during the rapid cooling of the melted powder;
- 4) Carbides are present inside the grains of the alloy and are probably formed on solidification;
- 5) The hardness values of the samples, higher than those reported in parts fabricated by different processes, are due to the presence of ϵ -lamellae grown on the $\{111\}_{\gamma}$ planes that restricts the dislocations slip in the γ (fcc) phase. Furthermore, slip in the ϵ -lamellae is inhibited by the intersection of these hcp lamellae with other hcp lamellae or with fcc regions.
- 6) The DMLS technique could be used to realize surgical implants, where a high degree of personalisation is required, saving money and time with respect to conventional procedures.

ACKNOWLEDGMENTS

This study was supported by the NAMABIO COST Action MP1005.

REFERENCES

- [1] A. Mazzoldi. Selective laser sintering in biomedical engineering. *Med Biol Eng Comput* 2013;51:245-256.
- [2] Lantada AD, Morgado PL. Rapid prototyping for biomedical engineering: current capabilities and challenges. *Annual Review of Biomedical Engineering* 2012;14:73-96.

420 [3] Rosochowski A, Matuszak A. Rapid tooling: the state of the art. J Mater Process Technol
421 2000;106:191-198.

422 [4] Hunt JA, Callaghan JT, Sutcliffe CJ, Morgan RH, Halford B, Black RA. The design and
423 production of Co-Cr alloy implants with controlled surface topography by CAD-CAM method
424 and their effects on osseointegration. Biomaterials 2005;26:5890-5897.

425 [5] Simchi A. Direct laser sintering of metal powders: Mechanism, kinetics and microstructural
426 features. Mater Sci Eng A 2006;428:148-158.

427 [6] Bassoli E, Gatto A, Iuliano L. Joining mechanisms and mechanical properties of PA
428 composites obtained by selective laser sintering. Rapid Prototyp J 2012;18:100-108.

429 [7] Gibson I, Cheung LK, Chow SP, Cheung WL, Beh SL, Savalani M, Lee SH. The use of rapid
430 prototyping to assist medical applications. Rapid Prototyp J 2006;12:53-58.

431 [8] Wang X, Yan Y, Zhang R. Rapid prototyping as a tool for manufacturing bioartificial livers.
432 Trends in Biotechnology 2007;25:505-513.

433 [9] Butscher A, Böhner M, Hofmann S, Gauckler L, Müller R. Structural and material
434 approaches to bone tissue engineering in powder-based three dimensional printing. Acta
435 Biomaterialia 2011;7:907-920.

436 [10] Atzeni E, Iuliano L, Minetola P, Salmi A. Proposal of an innovative benchmark for
437 accuracy evaluation of dental crown manufacturing. Computers in Biology and Medicine
438 2012;42:548-555.

439 [11] Davis JR. Nickel, Cobalt and Their Alloys Materials Park (OH): ASM
440 INTERNATIONAL;2000.

441 [12] Nasab MB, Hassan MR, Sahari BB. Metallic biomaterials of knee and hip - a review.
442 Trends Biomater. Artif. Organs 2010;24(2):69-82.

443 [13] Malayoglu U, Neville A. Mo and W as alloying elements in Co-based alloy – their effects
 444 on erosion – corrosion resistance. *Wear* 2005;259:219-229.

445 [14] Shin J, Doh J, Kim J. Effect of molybdenum on the microstructure and wear resistance of
 446 cobalt-base Stellite hardfacing alloys. *Surf Coat Technol* 2003;166:117-126.

447 [15] Davis JR, *Handbook of Materials for Medical Devices*: ASM International; 2003:21-50
 448 DOI: 10.1361/hmmd2003p013.

449 [16] Gaytan SM, Murr LE, Martinez E, Martinez JL, Machado BI, Ramirez DA, Medina F,
 450 Collins S, Wicher RB. Comparison of Microstructures and Mechanical Properties of Solid and
 451 Mesh Cobalt-base Alloy Prototypes Fabricated by Electron Beam Melting. *Metall Mater Trans*
 452 *A* 2010;41:3216-3227.

453 [17] Meacock CG, Vilar R. Structure and properties of a biomedical Co-Cr-Mo alloy produced
 454 by laser powder microdeposition. *J Laser Appl* 2009;21:88-95.

455 [18] Vandenbroucke B, Kruth JP. Selective laser melting of biocompatible metals for rapid
 456 manufacturing of medical parts. *Rapid Prototyp J* 2007;13:196-203.

457 [19] Averyanova M, Bertrand P, Verquin B. Manufacture of Co-Cr dental crowns and bridges by
 458 selective laser Melting technology. *Virtual Phys Prototyp* 2011;16:179-185.

459 [20] Reclaru L, Ardelean L, Rusu L, Sinescu C. Co-Cr material selection in prosthetic
 460 restoration: laser sintering technology. *Solid state phenomena* 2012;188:412-415.

461 [21] Cotrut CM, Ciucă S, Miculescu F, Antoniac I, Târcolea M, Vrânceanu DM. The influence
 462 of classical and modern manufacturing technologies on the properties of metal dental bridge.
 463 *Key engineering materials* 2014;583:163-168.

464 [22] Sanz C, Navas VG. Structural integrity of direct metal laser sintered parts subjected to
 465 thermal and finishing treatments. Journal of materials processing technology 2013;213:2126-
 466 2136.

467 [23] Saldivar-Garcia AJ, Lopez HF. Temperature effects on the lattice constants and crystal
 468 structure of a Co-27Cr-5Mo low-carbon alloy. Metall Mater Trans A 2004;35:2517-2523.

469 [24] Garcia JS, Medrano MA, Rodriguez AS. Formation of hcp martensite during the isothermal
 470 aging of an fcc Co-27Cr-5Mo-0.05C orthopedic implant alloy. Metall Mater Trans A
 471 1999;30:1177-1184.

472 [25] Rasband WS. ImageJ, U. S. National Institutes of Health, Bethesda, Maryland, USA,
 473 <http://imagej.nih.gov/ij/> 1997-2012.

474 [26] CrystalKitX version 1.9.1. Total Resolution LLC.

475 [27] Murr LE, Amato KN, Li SJ, Tian YX, Cheng XY, Gaytan SM, Martinez E, Shindo PW,
 476 Medina F, Wicker RB. Microstructure and mechanical properties of open-cellular biomaterials
 477 prototypes for total knee replacement implants fabricated by electron beam melting. J Mech
 478 Behav Biomed Mater 2011;4:1396-1411.

479 [28] Saldivar-Garcia AJ, Manì MA, Salinas RA. Effect of solution treatments on the fcc/hcp
 480 isothermal martensitic transformation in Co-27Cr-5Mo-0.05C aged at 800°C. Scr Mater
 481 1999;40:717-722.

482 [29] Lopez HF. Alloy developments in biomedical Co-base alloys for HIP implant applications.
 483 Materials science forum 2013;736:133-146.

484 [30] Vander Sande JB, Coke JR, Wulff J. A Transmission Electron Microscopy Study of the
 485 Mechanisms of Strengthening in Heat-Treated Co-Cr-Mo-C Alloys. Metall Trans A
 486 1976;7A:389-397.

- 487 [31] Song CB, Park HB, Seong HG, Lòpez HF. Development of a thermal ε -martensite in
488 atomized Co-Cr-Mo-C implant alloy powders. *Acta Biomaterialia* 2006;2:685-691.
- 489 [32] Lee SH, Nomura N, Chiba A. Significant improvement in mechanical properties of
490 biomedical Co-Cr-Mo alloys with combination of N addition and Cr-enrichment. *Mater Trans*
491 2008;49:260-264.
- 492 [33] Rajan K, Vander Sande JB. Room temperature strengthening mechanisms in a Co-Cr-Mo-C
493 alloy. *J Mater Sci* 1982;17:769-778.
- 494 [34] Gonzalez-Mora VA, Hoffmann M, Stroosnijder R, Gil FJ. The role of hardness and
495 roughness on the wear of different CoCrMo counterfaces on UHMWPE for artificial joints. *J*
496 *Biomedical Science and Engineering* 2011;4:651-656.